Rearrangement of secondary flow over spanwise heterogeneous roughness

A. Stroh[1,†]**, K. Schäfer**[1]**, B. Frohnapfel**[1] **and P. Forooghi**[1]

[1]Institute of Fluid Mechanics, Karlsruhe Institute of Technology, Karlsruhe, Germany

Turbulent flow over a surface with streamwise-elongated rough and smooth stripes is studied by means of direct numerical simulation (DNS) in a periodic plane open channel with fully resolved roughness. The goal is to understand how the mean height of roughness affects the characteristics of the secondary flow formed above a spanwise heterogeneous rough surface. To this end, while the statistical properties of roughness texture as well as the width and spacing of the rough stripes are kept constant, the elevation of the smooth stripes is systematically varied in different simulation cases. Utilizing this variation, three configurations – representing protruding, recessed and an intermediate type of roughness – are analysed. In all cases, secondary flows are present and the skin friction coefficients calculated for all the heterogeneous rough surfaces are meaningfully larger than what would result from the area-weighted average of those of homogeneous smooth and rough surfaces. This drag increase appears to be linked to the strength of the secondary flow. The rotational direction of the secondary motion is shown to depend on the relative surface elevation. The present results suggest that this rearrangement of the secondary flow is linked to the spatial distribution of the spanwise-wall-normal Reynolds stress component, which carries opposing signs for protruding and recessed roughness.

Key words: boundary layer structure, turbulent boundary layers, turbulence simulation

1. Introduction

Occurrence of a pronounced fluid motion perpendicular to the main flow direction has been observed in various wall-bounded flow configurations. Prandtl ([1931](#)) introduced the term secondary flows for this phenomenon and categorized them into three kinds. Secondary motions of Prandtl's second kind, which are in the focus of the present paper, occur in turbulent flows and are related to inhomogeneities of the Reynolds stresses. The classical example of this kind of secondary motion is flow in ducts with non-circular cross-sections, which was first reported by Nikuradse ([1926](#)).

† Email address for correspondence: alexander.stroh@kit.edu

In spite of its weak intensity, the secondary motion is known to be able to noticeably deform the primary mean velocity profile. Secondary flow of Prandtl's second kind can also occur in plane or symmetrical wall-bounded flows (i.e. channels or pipes) if a local spanwise inhomogeneity in wall conditions is present, due to, for example, surface roughness. The pioneering work by Hinze (1967, 1973) demonstrated the formation of secondary motions over flow-aligned roughness stripes in a duct with an upwelling motion above the smooth wall and a downwelling motion over the rough parts.

This phenomenon is particularly relevant in applications with spatially non-uniform roughness formation, a well-documented example being flow over turbomachinery blades (Bons *et al.* 2001). Experimental investigation of turbulent flow over a damaged turbine blade with irregular surface roughness by Mejia-Alvarez & Christensen (2013) and Barros & Christensen (2014) clearly showed the formation of secondary motions over such a blade surface. Another important manifestation of these secondary motions occurs in river flows, where lateral sediment transport can reinforce and maintain spanwise surface variations of longitudinal bedforms (Wang & Cheng 2006).

Despite the great variety of possible configurations with lateral wall inhomogeneity, two main configurations have been well studied in the recent decades: a spanwise variation in wall-shear stress and a spanwise variation of local elevation of the wall. Following Wang & Cheng (2006), we refer to the configuration where the former effect is dominant as strip-type roughness and to the latter as ridge-type roughness, respectively. These authors observed upwelling and downwelling motion in strip-type roughness to occur above the smooth and rough stripes, while for ridge-type roughness, the upwelling and downwelling motions were observed above the elevated and recessed wall areas, respectively.

Willingham *et al.* (2014) and Chung, Monty & Hutchins (2018) numerically studied idealized strip-type roughness in plane channels with stripes of low and high imposed friction drag on the wall surface. Both groups report a similar secondary flow to that observed by Hinze (1967, 1973) – that is, upwelling motion over the low-shear and downwelling motion over the high-shear region. This behaviour was linked to the experimental observations for flows over damaged turbine blades, for which Mejia-Alvarez & Christensen (2013) and Barros & Christensen (2014) identified regions with low and high mean streamwise velocity, termed as low- and high-momentum pathways (LMP and HMP), which are flanked by streamwise-oriented swirling motions (Anderson *et al.* 2015). In the study of Chung *et al.* (2018) it is shown that either LMP or HMP can be located above the high-shear stripe, depending on the spanwise extent of the stripe. For stripes of free-slip and no-slip boundary conditions, Türk *et al.* (2014) and Stroh *et al.* (2016) reported a switch of the secondary motion rotational sense through a variation of the spanwise extent of the free-slip region.

Ridge-type roughness has also been studied by various research groups. Goldstein & Tuan (1998) investigated secondary flow above riblets, concluding that it is mainly caused by the deflection of the spanwise velocity fluctuations. Vanderwel & Ganapathisubramani (2015) and Vanderwel *et al.* (2019) studied turbulent flow over streamwise-elongated rows of Lego blocks, both experimentally and numerically. Hwang & Lee (2018) employed DNS to examine the turbulent boundary layer over streamwise aligned ridges. All these groups observed an upwelling motion above the protruding surface areas.
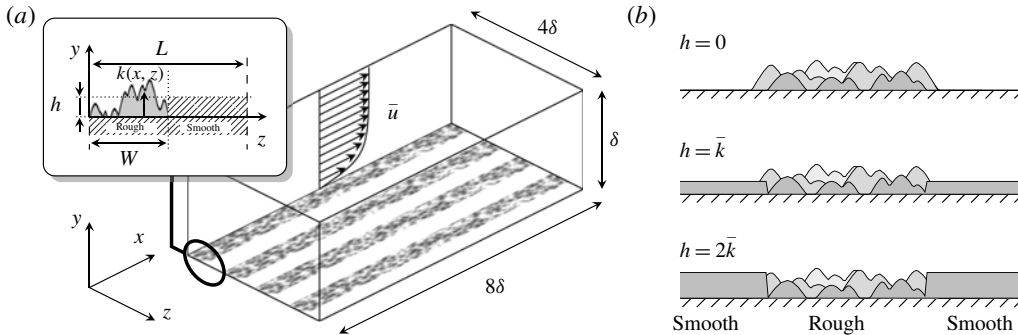
FIGURE 1. Schematic of the open channel numerical domain with roughness stripes at the walls (*a*) and introduced variation of the smooth wall elevation (*b*).

Despite the fact that reduction of the possible structure configuration to strip- and ridge-type roughness facilitates physical understanding by isolating the shear-increasing effect of the surface roughness from the effects linked to wall elevation, one should note that a clear-cut separation between the two categories is not necessarily possible for realistic roughness. The reason is that formation of roughness is inherently accompanied by a change in the surface height. This calls for an understanding of the conditions under which the behaviour of the secondary flow over a realistic roughness resembles that of each category. Such an open question deserves particular attention in the case of a protruding roughness, where the shear-inducing and height-increasing effects of roughness can cause opposing senses of rotation in the idealized scenarios.

The aim of the present work is to systematically investigate the effect of roughness mean height on secondary motions and thereby provide an understanding on the conditions under which a roughness stripe can be classified under ridge- or strip-type roughness. The effect of spanwise spacing is not part of this investigation. To this end we use DNS to study turbulent flow in an open channel with streamwise-elongated stripes of roughness, and at the same time systematically vary the mean height of roughness related to the smooth wall level. The roughness topography is nearly identical in statistical sense in all cases and the height difference is varied by shifting the smooth wall.

2. Procedure

A series of DNS has been carried out in a fully developed turbulent open channel flow driven by constant pressure gradient (CPG). The Navier–Stokes equations are numerically integrated using the spectral solver SIMSON (Chevalier *et al.* 2007), which employs Fourier decomposition in the horizontal directions and Chebyshev discretization in the wall-normal direction. A schematic of the numerical domain is depicted in figure 1(*a*). Periodic boundary conditions are applied in streamwise (*x*) and spanwise directions (*z*), while the wall-normal extension of the domain (*y*) is bounded by no-slip boundary conditions at the lower domain wall ($y = 0$) and symmetry boundary conditions ($v = 0$, $\partial u/\partial y = \partial w/\partial y = 0$) at the upper boundary ($y = \delta$). The numerical domain with a size of $(L_x \times L_y \times L_z) = (8\delta \times \delta \times 4\delta)$ is discretized with $768 \times 301 \times 384$ grid nodes, resulting in a spatial resolution of $(\Delta x^+ \times \Delta y^+_{min}, \Delta y^+_{max} \times \Delta z^+) = (5.2 \times 0.014, 2.6 \times 5.2)$. The velocity components
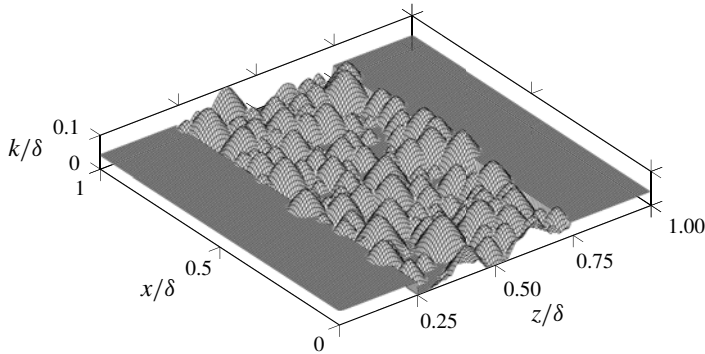
FIGURE 2. Zoomed view on the three-dimensional roughness distribution at $h = \bar{k}$.

in the streamwise, wall-normal and spanwise directions are denoted by (u, v, w), respectively.

Statistical integration in time and the streamwise direction is carried out over approximately 50 flow-through times for every considered simulation configuration. The initial transient after the introduction of a structured surface is excluded from this statistical integration – that is, the integration is started approximately two flow-through times after the bulk mean velocity reached a statistically steady state. The decomposition of the velocity field into a mean part and fluctuations, given as $u_i(x, y, z, t) = \bar{u}_i(y, z) + u'_i(x, y, z, t)$, is utilized. Hereby, the quantities averaged in the streamwise direction and time are denoted with an overbar $(\bar{\cdot})$, while angular brackets $\langle \cdot \rangle$ denote averaging in the spanwise direction. Additionally, based on the assumption of a symmetric velocity distribution with respect to the middle of the rough or the smooth surface stripes, we use those symmetries in the averaging procedure in order to obtain smoother statistical data.

The rough and elevated smooth surfaces are modelled by introduction of an external volume force field to the Navier–Stokes equations, based on the immersed boundary method proposed by Goldstein, Handler & Sirovich (1993). The presently used immersed boundary implementation has been validated in previous studies by Forooghi *et al.* (2018) and Vanderwel *et al.* (2019). The wavelength, L, represents the size of the alternating structure with a constant roughness fraction $\Phi = W/L = 0.5$, where W denotes the width of the rough area (figure 1a). Based on literature results (Vanderwel & Ganapathisubramani 2015; Chung *et al.* 2018; Hwang & Lee 2018) the wavelength $L/\delta = 1$ is considered, for which the formation of a strong large-scale secondary motion with pronounced LMP & HMP is expected. The rough surface is generated using the technique proposed by Forooghi *et al.* (2017), in which several discrete roughness elements are distributed randomly on the bottom surface, creating a rough surface with certain statistics. In the present simulations all roughness stripes have virtually the same statistical properties. Considering a homogeneous roughness, the statistical properties are as follows: mean elevation $\bar{k}/\delta = 0.043$, maximum peak elevation $k_{max}/\delta = 0.10$, root mean square elevation $k_{rms}/\delta = 0.024$, skewness $Sk = 0.079$ and kurtosis $Ku = 2.24$. One should note that these statistical properties belong to the rough areas and not the entire surface. Figure 2 shows a zoomed view of a roughness stripe for one of the cases $(h = \bar{k})$. As can be seen in the figure, there is a gradual transition from the smooth to the rough region. For this purpose, initially the elements are distributed on a wider area than the intended stripe

Case	δ_{eff}/δ	Re_τ	Re_b	U_b/U_b^s	U_b^+	c_f/c_f^s	$\left(\dfrac{\sqrt{\bar{v}^2+\bar{w}^2}}{U_b}\right)_{max}$	$\Omega_x\delta_{eff}^2/U_b^2$
Smooth	1.000	500.0	9051	1.000	18.1	1.00	—	—
$h=0$	0.978	499.9	5756	0.650	11.5	2.47	2.89×10^{-2}	1.46×10^{-3}
$h=\bar{k}$	0.958	499.9	5901	0.680	11.8	2.35	2.09×10^{-2}	0.57×10^{-3}
$h=2\bar{k}$	0.943	499.9	5699	0.668	11.4	2.52	3.03×10^{-2}	0.89×10^{-3}
Rough	0.957	500.0	5228	0.603	10.5	3.00	1.13×10^{-2}	0.19×10^{-3}

TABLE 1. Global flow properties for the considered configurations.

width W, and consequently, all the elements whose centres lie beyond the intended border are eliminated. As an additional reference case we also carry out a simulation where the entire wall area is uniformly covered by the rough surface. The border treatment at the edge of rough stripes slightly modifies the statistical properties of the roughness compared to the uniformly rough surface. Figure 1(*b*) shows the three considered elevations of the smooth surface: $h=0$, $\bar{k}$ and $2\bar{k}$. These three values might represent different roughness types (Bons *et al.* 2001): roughness generated by deposition ($h=0$, positively skewed, protruding roughness), roughness generated by simultaneous deposition and erosion ($h=\bar{k}$, near-zero skewness) and roughness generated by pitting, erosion or corrosion ($h=2\bar{k}$, negatively skewed, recessed or 'carved' roughness).

The friction Reynolds number in all simulations is fixed at $Re_\tau = \delta_{eff}/\delta_\nu = 500$ with the viscous length scale $\delta_\nu = \nu/u_\tau$, the friction velocity $u_\tau = \sqrt{\tau_{eff}/\rho}$ and the effective wall-shear stress $\tau_{eff} = -\delta_{eff}P_x$. The effective channel half-height $\delta_{eff} = \delta - h_{eff}$ (shown in table 1 for every configuration) takes into account the reduction of the cross-sectional area of the channel, where h_{eff} denotes the melt-down height of the entire introduced surface structure and P_x is the imposed streamwise pressure gradient. Due to the reduction of effective channel half-height for structured channels ($\delta_{eff} < \delta$) the identical friction Reynolds number (and hence the same scale separation) is maintained across all simulations by a reduction of δ_ν realized through an adjustment of the pressure gradient, so that $P_x = P_x^s(\delta/\delta_{eff})^3$, where P_x^s corresponds to the pressure gradient of the reference smooth channel simulation at $Re_\tau = 500$. Since Re_τ is fixed, the introduction of the structured surface into the flow field translates into a reduction of the bulk mean velocity $U_b = 1/(\delta_{eff}L_z) \int_0^{L_z} \int_0^\delta \bar{u}(y,z)\,\mathrm{d}y\,\mathrm{d}z$ and the corresponding bulk Reynolds number $Re_b = U_b\delta_{eff}/\nu$.

Throughout the manuscript the non-dimensionalization in viscous units is indicated by the superscript plus sign $(\cdot)^+$. It is performed using the friction velocity u_τ of the particular simulation. The superscript letters '*s*' and '*r*' denote the quantities of the smooth and homogeneous rough channel simulation, respectively. Extrinsic spatial averaging is utilized in the presented statistical datasets – that is, the solid regions (with zero velocity) are included into the averaging procedure.

3. Results

3.1. *Global flow properties*

Table 1 presents the global flow properties of the three considered heterogeneously rough configurations and compares them to a smooth and to a homogeneous rough channel flow. The spanwise heterogeneous rough surfaces, in which half of the
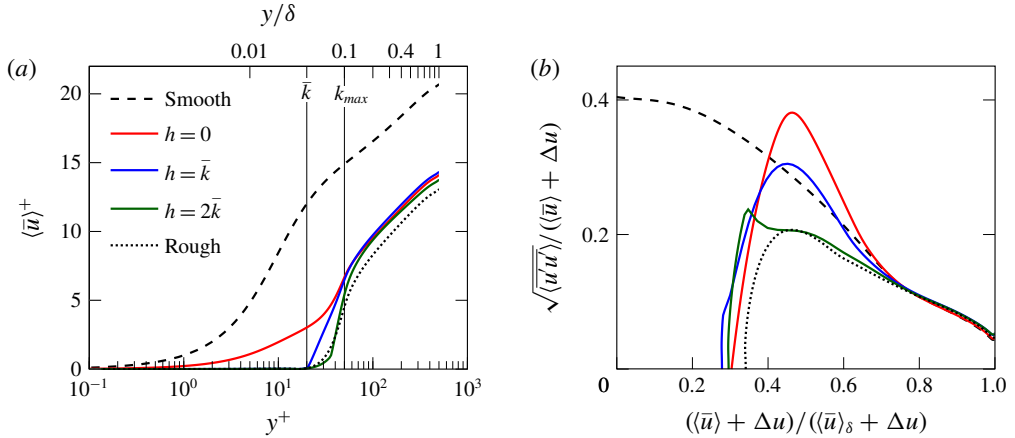
FIGURE 3. Mean velocity profile in inner scaling in logarithmic form (*a*) and diagnostic plot scaled with $\langle \bar{u} \rangle + \Delta u$ (*b*).

total surface is covered by roughness, exhibit a pronounced reduction of U_b by 32–35 % with respect to the smooth case, while the homogeneous rough surface yields a reduction of 40 %. The observed augmentation in skin friction coefficient, $c_f = 2u_\tau^2/U_b^2$, primarily originates from this reduction in bulk velocity.

If drag on the heterogeneous roughness could be calculated by superposition of the smooth and an entirely rough surface, which is arguably the asymptotic case when the stripes are extremely wide, the result would be $c_f = 0.5(c_f^s + c_f^r) = 2.00c_f^s$. In comparison to this asymptotic state, 24 %, 18 % and 26 % higher c_f is observed for $h = 0$, $\bar{k}$ and $2\bar{k}$, respectively, indicating a significant impact of secondary motions on skin friction drag as previously discussed, for example, by Türk *et al.* (2014) or Chung *et al.* (2018).

The strength of the secondary motion can be measured in terms of the maximal magnitude of the induced secondary motion $(\sqrt{\bar{v}^2 + \bar{w}^2}/U_b)_{max}$ or the specific mean streamwise enstrophy $\Omega_x = 1/A \int_0^{L_z} \int_0^\delta \bar{\omega}_x^2 \, \mathrm{d}y \, \mathrm{d}z$, where ω_x is the streamwise vorticity and A is the cross-sectional area of the flow field – i.e. $A = L_z \delta_{eff} = 4\delta\delta_{eff}$. The latter can be understood as a measure of the rotational energy contained in the secondary motions. Stroh *et al.* (2016) showed that a minimum of the specific enstrophy can be linked to the reversal of secondary flow direction in the case of stripes with slip and no-slip boundary conditions. This is also the case for the present data, as will be discussed later. The weakest secondary motion in the present work is observed for $h = \bar{k}$, which is also the case with the weakest drag increase. For the other two cases with similarly large drag increase, the secondary motion magnitude appears to be a better qualitative measure for the impact of the secondary flow on skin friction drag. It has to be noted that the homogeneous rough case also contains mean streamwise rotational energy, which is linked to the presence of local small-scale cross-sectional flows induced by roughness elements. The rotational energy content is, however, significantly smaller than the weakest secondary motion at $h = \bar{k}$, and its appearance is limited to the near-wall region slightly extending beyond $y = k_{max}$.

Figure 3(*a*) presents the inner-scaled mean velocity profiles in logarithmic form for the considered simulation configurations. The significant reduction of U_b and the corresponding downward shift of the logarithmic region of the profile is evident
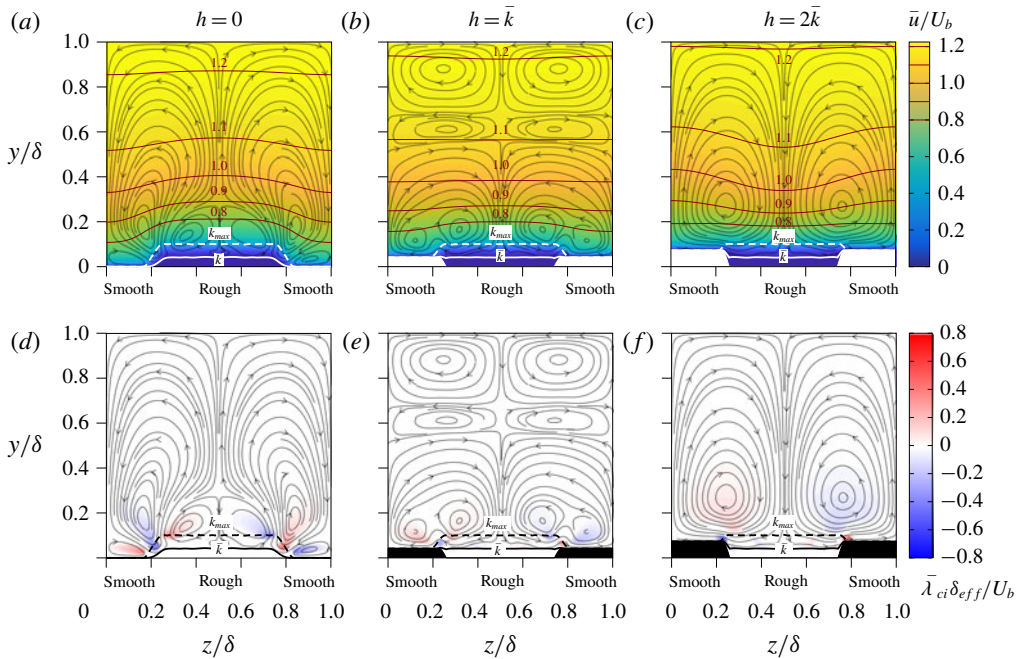
FIGURE 4. Mean velocity profile (*a–c*) and signed swirling strength (*d–f*) at different elevations of the smooth stripes h. Black lines indicate time-averaged streamlines of secondary motion in the y–z-plane; brown solid lines mark the isolines of the streamwise mean velocity distribution.

for all rough cases. In order to check whether these spanwise-averaged velocity profiles comply with outer layer similarity, we consider the diagnostic plot as introduced by Alfredsson & Örlü (2010) in the adapted version for rough surfaces as proposed by Castro, Segalini & Alfredsson (2013). To this end, the roughness function Δu is extracted from figure 3(*a*) and introduced in the normalization of the diagnostic function as shown in figure 3(*b*). In this representation the effects of absolute wall distance and wall-shear stress are excluded such that the dynamic similarity of turbulence intensity and mean velocity can directly be compared among all cases. It can be observed that the streamwise velocity fluctuations linearly scale with the local mean streamwise velocity in all considered configurations for $0.7 < (\langle \bar{u} \rangle + \Delta u)/(\langle \bar{u} \rangle_\delta + \Delta u) < 0.9$. In addition, all profiles collapse onto the smooth wall case in the outer region, thus indicating outer layer similarity of the different turbulent flows. As previously reported by Medjnoun, Vanderwel & Ganapathisubramani (2018), this suggests that the observed secondary motion alters the spanwise-averaged mean velocity profile and related turbulent fluctuations in the outer region in a similar manner for all considered simulations, independent of the roughness properties.

3.2. Secondary motion

Figure 4 presents the distribution of the mean velocity overlaid with the secondary flow (depicted by in-plane streamlines) for the three considered elevations of the smooth wall. In all three cases, pronounced secondary motion patterns can be

observed. In the case of $h = 0$ (figure 4a) the two main large-scale vortices originate from the edges of the rough ridge. Two additional counter-rotating small vortex pairs are located on the smooth wall and on top of the rough patch. The deformation of the streamwise velocity profile is shown with brown velocity isolines. It can be seen that a LMP is present over the rough surface part. This flow topology is similar to the secondary flows over ridge-type roughness (for example, Hwang & Lee (2018)).

In contrast, the case with $h = 2\bar{k}$ (figure 4c) shows a downward bulging of the streamwise velocity field, and thus HMP over the rough surface part. In this case the secondary motion is given through a single counter-rotating vortex pair with an upward motion above the elevated smooth region. This flow topology resembles the secondary flow reported for strip-type roughness (for example, Willingham *et al.* (2014) and Chung *et al.* (2018)).

The comparison of these two cases suggests that the alteration of the smooth wall elevation is an additional parameter for the secondary motion formation, which might enable rearrangement of the secondary flow topology from the ridge-type regime (LMP over rough area) to the strip-type regime (HMP over rough area).

The third case $h = \bar{k}$ (figure 4b) corresponds to an intermediate state between ridge- and strip-type roughness. In this flow a more complex secondary flow topology is present. The largest vortical structures do not cover the entire vertical domain and are significantly weaker, as indicated by the values listed in table 1. The streamwise enstrophy as well as the maximum magnitude of the secondary motion are lowest for this case. The rotational direction of the vortex pair in the lower channel half corresponds to the one observed for $h = 2\bar{k}$ and the small one located in the centre of the roughness for $h = 0$.

Note that even though the bulging pattern of the mean streamwise velocity contours is different in the three cases, it is not so strong as to disturb the similarity of the velocity defect profiles depicted in figure 3(b). This finding is in agreement with the suggestion by Chung *et al.* (2018) that a departure from the global outer layer similarity – or laterally uniform regime as referred to by these authors – occurs when the ratio of roughness spacing to channel half-height, W/δ, exceeds a threshold that is between 0.39 and 0.79; the present value is 0.5.

3.3. *Turbulent flow properties*

For typical rough surfaces, shear stress and turbulent kinetic energy (TKE) in the vicinity of roughness is higher compared to a smooth wall at the same flow rate. In the case of laterally heterogeneous roughness, spanwise gradients of these quantities are typically related to the occurrence of secondary motions (Barros & Christensen 2014) even though it is still an open issue in literature whether HMP or LMP are located over high-shear stress regions (Chung *et al.* 2018).

Figure 5 shows the spanwise variation of total shear stress, $\bar{\tau}_{xy} = \mu(\mathrm{d}\bar{u}/\mathrm{d}y) - \rho\overline{u'v'}$, and turbulent kinetic energy, $\bar{K} = 0.5(\overline{u'u'} + \overline{v'v'} + \overline{w'w'})$, for all three cases of the present investigation at the same wall-normal location. It can be seen that all roughness stripes yield a similar distribution of total shear stress and TKE, in the sense that the regions with high levels of these quantities are always located above the rough stripes. Thus these flows are indeed examples where either HMP or LMP can be located above the high-shear stress region, depending on the relative height of the roughness. It can be deduced that spatial gradients of TKE or shear stress are not directly linked to the rotational direction of the largest secondary motion and the related occurrence of HMP and LMP in these cases. At the same time it should
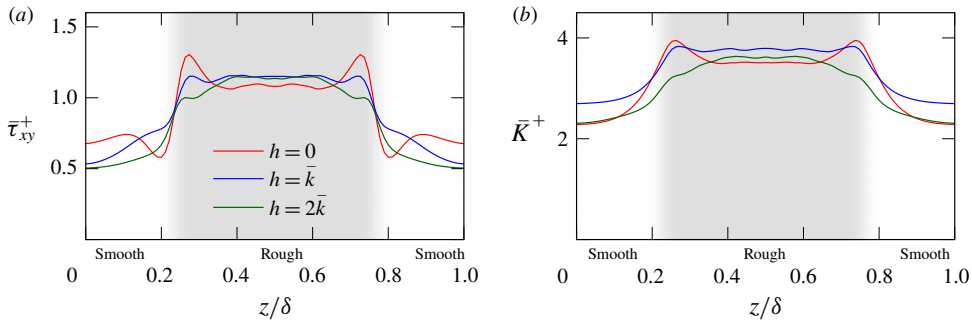
FIGURE 5. Total stress (*a*) and turbulent kinetic energy (*b*) extracted at $y = k_{max} = 0.1\delta$ for the three different elevations of the smooth stripes.
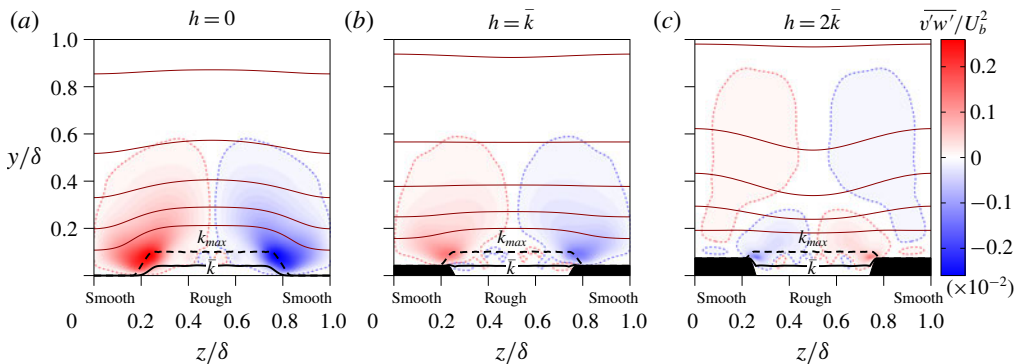

FIGURE 6. Reynolds stress $\overline{v'w'}$ at different elevations of the smooth stripes h. Brown solid lines mark the isolines for the streamwise mean velocity distribution with isolevels corresponding to figure 4.

be noted that the secondary motions directly above the rough stripes are similar for all three cases, as they all generate a spanwise mean flow from the middle of the roughness patch towards its edges (see figure 4), which agrees with the rotational direction reported for strip-type roughness. This secondary motion appears to be strengthened further in the case of $h = 2\bar{k}$, while an opposing secondary motion, originating from the edges of the rough patch, dominates the case $h = 0$.

Regarding the edge of protruding surface structures, Hwang & Lee (2018) identified the wall-normal deflection of spanwise velocity fluctuations at this location – which results in a strong correlation of spanwise and wall-normal velocity fluctuations, i.e. $\overline{v'w'}$ – as an important quantity for the formation of secondary motions. The $\overline{v'w'}$ Reynolds stress, and in particular its spatial gradients, were also found to be important for the rearrangement of secondary flows over slip/no-slip stripes with varying width (Stroh *et al.* 2016).

Figure 6 shows the spatial distribution of $\overline{v'w'}$ for the present cases. The magnitude of $\overline{v'w'}$ is strongest for $h = 0$ and a switch of sign above the rough surface stripe can be seen for $h = 2\bar{k}$. The distribution for $h = 2\bar{k}$ corresponds to the one found over strip-type roughness (Chung *et al.* 2018), while the distribution for $h = 0$ is in good agreement with the studies of ridge-type roughness (Hwang & Lee 2018;

Vanderwel *et al.* 2019). The opposing signs of $\overline{v'w'}$ for $h = 0$ and $h = 2\bar{k}$ around the smooth–rough transition location can be directly related to the different deflection of spanwise velocity fluctuations. The sign of the generated correlation between v' and w' differs above the rough to smooth transition, depending on whether the roughness or the smooth part of the wall forms the protruding surface.

In the case of the recessed roughness ($h = 2\bar{k}$) the deflection on the protruding smooth surface part supports the $\overline{v'w'}$ distribution found on non-elevated surfaces with increased drag. In consequence, only one pair of secondary vortices is present, which coincides with the one found for strip-type roughness. For the protruding roughness ($h = 0$), on the other hand, the $\overline{v'w'}$ distribution opposes the one for strip-type roughness. In the present case, this influence of the local mean surface elevation dominates the secondary flow formation, and thus yields a different rotational direction than for $h = 2\bar{k}$. For the case with $h = \bar{k}$, where the melt-down height of the roughness is the same as the smooth surface height, the $\overline{v'w'}$ distribution appears to be dominated by the protruding parts of the surface roughness for the present geometry. At the same time its influence on the secondary flow formation appears to be weak. Overall, the present results suggest that the variation of rotational direction for different roughness heights is strongly related to the difference in the introduced wall-normal deflections of spanwise velocity fluctuations.

4. Conclusions

DNS of turbulent flow over alternating, streamwise-elongated, rough and smooth stripes are presented. The roughness is fully resolved numerically by means of an immersed boundary method. While the statistical properties of the roughness texture as well as the width and spacing of the rough areas are kept constant, the elevation of the smooth wall is systematically varied. This set-up allows identifying the relevance of protruding or recessed roughness for the secondary flow formation. In addition, it couples the effect of lateral drag variation and relative roughness elevation, whose effects on the secondary flow formation have been mostly studied separately in literature up to now (strip-type roughness versus ridge-type roughness).

The obtained results reveal opposite rotational directions for the same type of roughness topography, depending on whether it is introduced as protruding roughness ($h = 0$) or recessed roughness ($h = 2\bar{k}$). While the drag on the rough surface stripes is always larger than on the smooth stripes, the secondary flow induces low-speed regions above the protruding roughness, in contrast to high-speed regions above the recessed roughness. Thus the secondary flow caused by protruding roughness stripes is similar to the behaviour previously reported for ridge-type roughness, while that for a recessed roughness resembles the one over strip-type roughness. An intermediate case in which the mean roughness height is identical to the smooth wall position ($h = \bar{k}$) resembles the one for strip-type roughness to some extent, and produces significantly weaker secondary motion than the two other cases. The global drag on all heterogeneous rough surfaces is significantly larger than the area-weighted superposition of the smooth and rough values would suggest. This drag increase appears to be related to the strength of the secondary motion.

Since the areas with high turbulent kinetic energy and total shear stress are concentrated above the rough stripes for all investigated cases, these quantities cannot be directly related to the observed switch in rotational direction. The turbulence property that is found to be related to this switch is the $\overline{v'w'}$ Reynolds stress component. This quantity, which is related to the transport of turbulent kinetic

energy (Hwang & Lee 2018) and whose spatial gradients occur in the mean momentum budget for $\overline{v}$ and $\overline{w}$ (Stroh *et al.* 2016), switches sign in agreement with the rotational direction of the secondary motion. This sign switch is related to the relative roughness height through the different deflections that spanwise velocity fluctuations experience for protruding or recessed roughness. For recessed roughness the generated $\overline{v'w'}$-distribution is similar to the one for idealized strip-type roughness. Therefore, an elevated smooth surface part potentially enhances the strength of the secondary motion. For protruding roughness the deflections at the rough–smooth transition are such that a competing mechanism for the secondary flow formation is generated. With increasing roughness height this effect is increasingly dominant and can generate a switch of the large-scale rotational direction of the secondary motion. Thus the relative roughness height is identified as a key quantity for the rotational direction of secondary flow over spanwise heterogeneous roughness. We note that this effect might be less pronounced in high-Reynolds-number flows, for which the ratio k_{max}/δ can be significantly smaller. This issue should be addressed in future experimental studies.

Finally, the present results suggest that it could be possible to control the strength and rotational direction of the secondary motions above inhomogeneous rough surfaces through the relative roughness elevation. Such a control option is highly interesting, since the induced secondary motions indicate a significant global drag increase irrespective of their rotational direction, while a minimum of drag increase is expected for the transition between protruding and recessed roughness. It remains to be tested in future studies which minimal drag can be achieved for inhomogeneous rough surfaces through minimization of the secondary motions.

Acknowledgements

Declaration of interests

The authors report no conflict of interest.

References

ALFREDSSON, P. H. & ÖRLÜ, R. 2010 The diagnostic plot – a litmus test for wall bounded turbulence data. *Eur. J. Mech.* (B/*Fluids*) **29** (6), 403–406.

ANDERSON, W., BARROS, J. M., CHRISTENSEN, K. T. & AWASTHI, A. 2015 Numerical and experimental study of mechanisms responsible for turbulent secondary flows in boundary layer flows over spanwise heterogeneous roughness. *J. Fluid Mech.* **768**, 316–347.

BARROS, J. M. & CHRISTENSEN, K. T. 2014 Observations of turbulent secondary flows in a rough-wall boundary layer. *J. Fluid Mech.* **748**, R1.

BONS, J., TAYLOR, R., MCCLAIN, S. & RIVIR, R. 2001 The many faces of turbine surface roughness. In *ASME Turbo Expo 2001: Power for Land, Sea, and Air*, pp. V003T01A042–V003T01A042. American Society of Mechanical Engineers.

CASTRO, I. P., SEGALINI, A. & ALFREDSSON, P. H. 2013 Outer-layer turbulence intensities in smooth- and rough-wall boundary layers. *J. Fluid Mech.* **727**, 119–131.

CHEVALIER, M., SCHLATTER, P., LUNDBLADH, A. & HENNINGSON, D. S. 2007 Simson – A pseudo-spectral solver for incompressible boundary layer flows. *Tech. Rep.* TRITA-MEK 2007-07. KTH Stockholm, Stockholm, Sweden.

CHUNG, D., MONTY, J. P. & HUTCHINS, N. 2018 Similarity and structure of wall turbulence with lateral wall shear stress variations. *J. Fluid Mech.* **847**, 591–613.

FOROOGHI, P., STROH, A., MAGAGNATO, F., JAKIRLIĆ, S. & FROHNAPFEL, B. 2017 Toward a universal roughness correlation. *Trans. ASME J. Fluids Engng* **139** (12), 121201.

FOROOGHI, P., STROH, A., SCHLATTER, P. & FROHNAPFEL, B. 2018 Direct numerical simulation of flow over dissimilar, randomly distributed roughness elements: a systematic study on the effect of surface morphology on turbulence. *Phys. Rev. Fluids* **3** (4), 044605.

GOLDSTEIN, D., HANDLER, R. & SIROVICH, L. 1993 Modeling a no-slip flow boundary with an external force field. *J. Comput. Phys.* **105** (2), 354–366.

GOLDSTEIN, D. B. & TUAN, T.-C. 1998 Secondary flow induced by riblets. *J. Fluid Mech.* **363**, 115–151.

HINZE, J. O. 1967 Secondary currents in wall turbulence. *Phys. Fluids* **10** (9), S122–S125.

HINZE, J. O. 1973 Experimental investigation on secondary currents in the turbulent flow through a straight conduit. *Appl. Sci. Res.* **28** (1), 453–465.

HWANG, H. & LEE, J. 2018 Secondary flows in turbulent boundary layers over longitudinal surface roughness. *Phys. Rev. Fluids* **3** (1), 014608.

MEDJNOUN, T., VANDERWEL, C. & GANAPATHISUBRAMANI, B. 2018 Characteristics of turbulent boundary layers over smooth surfaces with spanwise heterogeneities. *J. Fluid Mech.* **838**, 516–543.

MEJIA-ALVAREZ, R. & CHRISTENSEN, K. T. 2013 Wall-parallel stereo particle-image velocimetry measurements in the roughness sublayer of turbulent flow overlying highly irregular roughness. *Phys. Fluids* **25** (11), 115109.

NIKURADSE, J. 1926 *Untersuchung über die Geschwindigkeitsverteilung in turbulenten Strömungen*. VDI-Verlag.

PRANDTL, L. 1931 *Einführung in die Grundbegriffe der Strömungslehre*. Akademische Verlagsgesellschaft.

STROH, A., HASEGAWA, Y., KRIEGSEIS, J. & FROHNAPFEL, B. 2016 Secondary vortices over surfaces with spanwise varying drag. *J. Turbul.* **17** (12), 1142–1158.

TÜRK, S., DASCHIEL, G., STROH, A., HASEGAWA, Y. & FROHNAPFEL, B. 2014 Turbulent flow over superhydrophobic surfaces with streamwise grooves. *J. Fluid Mech.* **747**, 186–217.

VANDERWEL, C. & GANAPATHISUBRAMANI, B. 2015 Effects of spanwise spacing on large-scale secondary flows in rough-wall turbulent boundary layers. *J. Fluid Mech.* **774**, 1–12.

VANDERWEL, C., STROH, A., KRIEGSEIS, J., FROHNAPFEL, B. & GANAPATHISUBRAMANI, B. 2019 The instantaneous structure of secondary flows in turbulent boundary layers. *J. Fluid Mech.* **862**, 845–870.

WANG, Z.-Q. & CHENG, N.-S. 2006 Time-mean structure of secondary flows in open channel with longitudinal bedforms. *Adv. Water Resour.* **29** (11), 1634–1649.

WILLINGHAM, D., ANDERSON, W., CHRISTENSEN, K. T. & BARROS, J. M. 2014 Turbulent boundary layer flow over transverse aerodynamic roughness transitions: induced mixing and flow characterization. *Phys. Fluids* **26** (2), 025111.